

# X-ray emission and internal kinematics in early-type galaxies. I. Observations<sup>\*</sup>

S. Pellegrini,<sup>1</sup> E. V. Held,<sup>2,3</sup> and L. Ciotti<sup>2</sup>

<sup>1</sup> *Dipartimento di Astronomia, Università di Bologna, via Zamboni 33, I-40126 Bologna, Italy*

<sup>2</sup> *Osservatorio Astronomico di Bologna, via Zamboni 33, I-40126 Bologna, Italy*

<sup>3</sup> *Osservatorio Astronomico di Padova, vicolo dell'Osservatorio 5, I-35122 Padova, Italy*

## ABSTRACT

Long slit spectroscopic data for 7 early-type galaxies with X-ray emission have been analyzed to derive velocity dispersion and radial velocity profiles. Major axis rotation curves out to  $R \sim R_e$  are presented. Adding these new data to those available in the literature, we have built a sample of early-type galaxies with detected X-ray emission and known kinematics (central velocity dispersion  $\sigma_c$  and maximum rotational velocity  $v_{\text{rot}}$ ). This sample is used to investigate from an observational point of view the role of rotation and flattening on the X-ray emission, particularly with regard to the X-ray underluminosity of flat systems.

The trend between the X-ray to optical ratio  $L_X/L_B$ , a measure of the hot gas content of the galaxies, and  $v_{\text{rot}}/\sigma_c$  is L-shaped, with the X-ray brightest objects confined at  $v_{\text{rot}}/\sigma_c \lesssim 0.4$ , both for Es and S0s. Neither for low or intermediate, nor for high  $L_X/L_B$ , there is any clear correlation between X-ray emission and rotational properties. The trend between  $L_X/L_B$  and the ellipticity  $\epsilon$  is also L-shaped, and resembles that between  $L_X/L_B$  and  $v_{\text{rot}}/\sigma_c$ : there are no high  $L_X/L_B$  objects with high  $\epsilon$ . The relationships between  $L_X/L_B$ , the anisotropy parameter  $(v/\sigma)^*$ , and the isophotal shape parameter  $a_4/a$  have also been investigated, but no significant trends have been found.

The existence of a relation between  $v_{\text{rot}}/\sigma_c$  and  $\epsilon$  makes it difficult to assess on a purely observational ground whether rotation or flattening is at the basis of the L-shaped trends found, although the trend with  $v_{\text{rot}}/\sigma_c$  is sharper than that with  $\epsilon$ . Our observational findings are then discussed in connection with the effects that rotation and flattening are predicted to have in the steady state cooling flow and in the evolutionary wind/outflow/inflow scenarios for the hot gas behavior.

**Key words:** galaxies: elliptical and lenticular, cD – galaxies: ISM – galaxies: kinematics and dynamics – galaxies: structure – X-rays: galaxies

## 1 INTRODUCTION

X-ray observations, beginning with the *Einstein* Observatory, have demonstrated that normal early-type galaxies are X-ray emitters, with 0.2–4 keV luminosities ranging from  $\sim 10^{40}$  to  $\sim 10^{43}$  erg s<sup>-1</sup> (Fabbiano 1989; Fabbiano, Kim & Trinchieri 1992). The X-ray luminosity  $L_X$  is found to correlate with the blue luminosity  $L_B$  ( $L_X \propto L_B^{2.0 \pm 0.2}$ ), although there is a large scatter of roughly two orders of magnitude in  $L_X$  at any fixed  $L_B > 3 \times 10^{10} L_\odot$ . The observed X-ray spectra of high  $L_X/L_B$  galaxies are consistent with thermal emission from hot, optically thin gas, while those of low  $L_X/L_B$  objects can be mostly accounted for by emission from stellar sources (Kim, Fabbiano & Trinchieri 1992). The scatter in the  $L_X - L_B$  diagram has been recognized as the most

striking feature of the X-ray properties of early-type galaxies. It was originally explained in terms of environmental differences (e.g., White & Sarazin 1991), or in terms of different dynamical phases for the hot gas flows, ranging from winds to subsonic outflows to inflows, going from the lowest to the highest  $L_X/L_B$  values (Ciotti et al. 1991, hereafter WOI scenario).

Recent observational results, followed by new theoretical work, have produced a new debate on the explanation of the scatter. Eskridge, Fabbiano & Kim (1995a,b; hereafter EFKa,b) conducted a multivariate statistical analysis of data measuring the optical and X-ray properties of the *Einstein* sample of early-type galaxies, the largest X-ray-selected sample of such galaxies presently available. They showed that on average S0 galaxies have lower  $L_X$  and  $L_X/L_B$  at any fixed  $L_B$  than do ellipticals. Moreover they found that galaxies with axial ratio close to unity span the full range of  $L_X$ , while flat systems all have  $L_X \lesssim 10^{41}$  erg s<sup>-1</sup>. The relationship defined by  $L_X/L_B$  is stronger than

<sup>\*</sup>Based on observations collected at the European Southern Observatory, La Silla, Chile

that defined by  $L_X$ , and it is in the sense that at any fixed  $L_B$  the X-ray-brightest galaxies are also the roundest. This correlation holds for both morphological subsets of Es and S0s.

These new observational findings have been followed by theoretical studies concerning the role played by the shape of the mass distribution and by galactic rotation in producing a different  $L_X$ , at fixed  $L_B$  (Kley & Mathews 1995; Ciotti & Pellegrini 1996, hereafter CP; Brighenti & Mathews 1996, hereafter BM; D’Ercole & Ciotti 1996). The different views of these authors, and their different predictions, will be presented in Section 6.

In this paper we focus on the effect of galactic rotation on  $L_X$ , from an observational point of view. We have built the first sample of early-type galaxies for which  $L_X$ , the maximum rotational velocity  $v_{\text{rot}}$ , and the central velocity dispersion  $\sigma_c$  are known, collecting data from the literature, and performing ourselves new long-slit spectroscopic observations for 7 galaxies. The resulting sample consists of 52 galaxies. In a subsequent paper (Paper II) we build the mass models specific for two galaxies with kinematic and photometric data obtained by us, and then we perform hydrodynamical simulations for such models.

This paper is organized as follows. In Section 2 we present our sample, in Section 3 we describe the details of the observations, in Section 4 we briefly summarize the reduction and analysis procedures, in Section 5 we present the results of our observations, in Section 6 we discuss the different theoretical scenarios in relation with the observational data, and in Section 7 we present our conclusions.

## 2 SAMPLE SELECTION

Our aim is to investigate the role of rotation in the X-ray luminosity of early-type galaxies. The sample of early-type galaxies with X-ray emission detected by the *Einstein* satellite is made of 67 objects (Fabbiano et al. 1992); the radial velocity  $v$  has already been measured for 45 of these. We obtained measurements of velocity dispersion  $\sigma$  and radial velocity  $v$  along the major axis for a sample of 7 more Es and S0s belonging to the Fabbiano et al. (1992) catalog, and for which there are no published kinematic data, at least describing their rotational properties. These are three S0s (NGC 2563, NGC 4526, NGC 4753), three ellipticals (NGC 3078, NGC 3258, NGC 3923), and one E/S0 (NGC 4756). The main characteristics of the observed galaxies (classifications, total magnitudes, effective radii, position angles, etc.) are summarized in Table 1. Our goal was to obtain major axis spectra with good S/N ratio down to  $\sim 0.5R_e$ , within which typical early-type galaxies reach their maximum rotation velocities (e.g., Fried & Illingworth 1994).

## 3 OBSERVATIONS

Our long-slit spectroscopic observations were taken with the Boller & Chivens spectrograph attached at the Cassegrain focus of the ESO 1.52 m telescope at La Silla, on February 25 and 26, 1995. Details of the instrumental setup are given in Table 2. The wavelength resolution (FWHM) is  $1.8\text{\AA}$ , equivalent to velocity dispersions of  $\sim 50\text{ km s}^{-1}$  at  $5000\text{\AA}$ .

The observations are listed in Table 3. The majority of them were made with the slit centered on the galaxy nucleus, and aligned along the photometric major axis. In one case, NGC 2563, a spectrum was also taken along the minor axis. To better sample the most extended galaxies, NGC 4526 and NGC 4753, and to better estimate the sky background – which is derived from the same exposure made for the galaxies, using a region in their outskirts – two series of exposures were made: in one series the slit included the nucleus and one end of the major axis, in the other it included the nucleus and the opposite end (see also Table 3). Right before and after each galaxy exposure a He-Ar arc lamp spectrum was obtained for calibration purposes; the instrument proved to be very stable. Flat field frames, dark and bias frames were taken during the day. Four different template stars with spectral types K0III to K3III were observed each night.

## 4 REDUCTION AND ANALYSIS

### 4.1 Calibration

The reduction steps were carried out with the IRAF package, and included: subtraction of bias, flat-field division, wavelength calibration and correction for the geometrical distortion (along the dispersion direction), sky subtraction, correction for bad pixels and removal of cosmic ray events. Wavelength calibration was obtained by fitting a fifth-order polynomial to  $\sim 25$  spectral lines from the He-Ar arc lamp spectra. The residual systematic deviations from the fitted polynomials were typically less than  $0.05\text{\AA}$ , and were uncorrelated from line to line.

The tilt of the spectrum was measured by mapping the centroid of the light distribution along the slit, and a polynomial was fitted. The geometrical corrections to be applied were found to be small (within 1–2 pixel); residual distortions are within  $\pm 0.05$  pixels for the standard stars, and within  $\pm 0.3$  pixel for the galaxies. The end product was a two-dimensional spectrum, binned logarithmically in the wavelength direction, and linearly in the spatial one. Finally, the night sky spectrum was determined for each galaxy from the outer ends of each spectrum, and subtracted from the image.

### 4.2 Radial velocities and velocity dispersions

The spectra have been analyzed using the Fourier Fitting method (Franx et al. 1989) to derive velocity dispersion and radial velocity profiles. This technique adds spectra along the slit until the specified S/N ratio is achieved, subtracts the continuum, filters out of the Fourier transformed spectrum the low and high wavenumbers, fits the galaxy spectrum to the stellar spectrum to determine a gaussian broadening function. Changing the template star or the spectral range produced changes in our results well within the formal errors given by the method.

Independent radial velocities have also been found using the restricted Fourier method (i.e., with the broadening function kept constant), which is similar to the cross-correlation method. In the outer regions of the galaxies, whenever the S/N was too low for a good determination

**Table 1.** Observed Galaxies

Galaxy	Type RSA, RC3	B mag	$\log(L_B)$ $L_\odot$	$\log(L_X)$ erg s <sup>-1</sup>	$\log(L_X/L_B)$ erg s <sup>-1</sup> / $L_\odot$	$\sigma_c$ km s <sup>-1</sup>	PA deg	d Mpc	$R_e$ "	$b/a$
(1)	(2)	(3)	(4)	(5)	(6)	(7)	(8)	(9)	(10)	(11)
NGC 2563	EL <sup>a</sup> , S0	13.01	10.95	42.12	31.17	260	80	96.1	19.37	0.72
NGC 3078	E3, E2+	11.86	10.91	41.17	30.26	237	177	53.7	22.76	0.83
NGC 3258	E1, E1	12.14	10.90	41.48	30.58	271	75	60.3	30.00	0.85
NGC 3923	E4/S0, E4-5	10.27	11.32	41.35	30.03	241	50	41.5	49.79	0.66
NGC 4526	S0, S0	10.54	10.84	40.14	29.30	267	113	27.0	44.37	0.33
NGC 4753	S0, I0	10.53	10.75	40.08	29.33		80	24.3	45.41	0.47
NGC 4756	E3, SAB0	13.27	10.78	42.06	31.28		50	88.4	16.49	0.49

Notes – Col. (2) gives the classifications of the galaxies from Sandage & Tammann (1987) (RSA), and from de Vaucouleurs et al. (1991) (RC3); the total B magnitude in col. (3) is  $B_T^0$  from RC3.  $L_B$  in col. (4) has been derived using distances listed in col. (9), which are given in Fabbiano et al. (1992); these are taken from Tully (1988), or are estimated from the CfA redshift survey data; a Hubble constant of 50 km s<sup>-1</sup> Mpc<sup>-1</sup> is assumed. The X-ray luminosity in col. (5) is from Fabbiano et al. (1992), and  $L_X/L_B$  in col. (6) has been estimated from cols. (4) and (5). The central velocity dispersion in col. (7) is from the catalog of McElroy (1995). The position angle of the major axis in col. (8) is from RC3, as are the effective radius in col. (10), and the minor to major axes ratio in col. (11). <sup>a</sup> EL = elliptical or lenticular.

**Figure 1.** The radial velocity profiles and velocity dispersion profiles, in km s<sup>-1</sup>, for the observed galaxies. The profiles are folded with respect to the center. Error bars represent the formal error estimate of the Fourier Fitting program. Thick marks on the upper abscissa axes in the  $\sigma$ 's plots are placed at  $0.5a_e$ , that is derived from  $R_e$  of Table 1 using the formula  $R_e^2 = (1 - \epsilon)a_e^2$ , where  $\epsilon = 1 - b/a$ , and constant ellipticity with radius is assumed. Open symbols are data SW of the nucleus, and filled ones NE, for NGC 2563 (major axis), NGC 3258, NGC 3923, NGC 4756, NGC 4753; open symbols are SE, and filled ones NW, for NGC 4526, NGC 3078. All the data are tabulated in Appendix A.

**Figure 1 – continued**

of  $\sigma$ , this procedure was useful to obtain more secure determinations of  $v$ . Radial velocities have been determined out to a radius where the scatter in the results – when varying the template star or the parameters of the analysis – was well within the formal errors.

## 5 RESULTS

The final radial velocity and velocity dispersion profiles for our program galaxies are plotted in Fig. 1. The kinematic data are tabulated in Appendix A. The zero points of the radial scales are those that give the maximum symmetry of the rotation curves on the two sides of the major axis; these centers are always close to the row of maximum intensity in the light profile of the galaxies (when they differ, the shift

is at most of 3 pixels). The solid lines shown in some of the radial velocity plots in Fig. 1 are the best fit curves of the shape (Franx et al. 1989)

$$v = v_0 \frac{R}{r_s + |R|}. \quad (1)$$

From the best model fit the velocity in the outermost observed region was determined; this is tabulated in Table 4. In this table we also list  $v_{\text{rot}}$ , i.e., the error weighted mean rotational velocities calculated over the region where the rotation curve is mostly flat. Typically we could determine the radial velocity profile out to  $R \sim R_e$ .

Finally, we have derived average dispersions from the center to half effective major axis  $a_e$  (the major axis of the ellipse within which one-half of the total B-band flux

**Table 2.** Instrumental parameters

CCD characteristics:	
CCD .....	#24 FA 2048L (1pix=15 $\mu$ )
Read-out-noise .....	5.24 e <sup>-</sup> pix <sup>-1</sup>
Conversion factor .....	2.90 e <sup>-</sup> /ADU
SLIT characteristics:	
spatial scale .....	0''.81 pix <sup>-1</sup>
slit length .....	4'1
slit width .....	2''
grating .....	#10 2nd order
dispersion .....	65.1 Å mm <sup>-1</sup>
spectral range .....	4300–6300 Å
resolution – FWHM .....	1.8Å
seeing .....	1''.1–1''.4
resolution <sup>a</sup> $\sigma_i$ .....	~ 50 km s <sup>-1</sup>

<sup>a</sup> Instrumental dispersion, determined as an average of the sigma's of Gaussian fits to lines in calibration spectra and to sky emission lines, and calculated at 5000 Å.

**Table 3.** Observations

Galaxy	$t_{int}$	date	PA
(1)	(2)	(3)	(4)
NGC 2563	40	2/25/1995	-10 <sup>a</sup>
NGC 2563	40	2/25/1995	80
NGC 2563	40	2/25/1995	80
NGC 3078	35	2/26/1995	-3
NGC 3258	40	2/25/1995	75
NGC 3258	40	2/25/1995	75
NGC 3923	35	2/26/1995	50
NGC 4526 SE	35	2/25/1995	75 <sup>b</sup>
NGC 4526 SE	35	2/25/1995	75 <sup>b</sup>
NGC 4526 NW	32	2/25/1995	75 <sup>c</sup>
NGC 4526 NW	30	2/25/1995	75 <sup>c</sup>
NGC 4753 SW	28	2/26/1995	80 <sup>d</sup>
NGC 4753 SW	24	2/26/1995	80 <sup>d</sup>
NGC 4753 NE	28	2/26/1995	80 <sup>e</sup>
NGC 4753 NE	24	2/26/1995	80 <sup>e</sup>
NGC 4756	40	2/26/1995	50
NGC 4756	40	2/26/1995	50

Notes – Col. (2) gives the integration time in minutes, col. (3) gives the date of the observations, col. (4) gives the input position angle (in degrees from N to E) at the telescope. When not specified, the slit was aligned along the photometric major axis, given in col. (7) in Table 1. <sup>a</sup>Minor axis. <sup>b</sup>The slit contains the nucleus and the SE direction of the major axis. <sup>c</sup>The slit contains the nucleus and the NW direction; <sup>d</sup>the nucleus and the SW direction; <sup>e</sup>the nucleus and the NE direction.

is emitted). Central velocity dispersions  $\sigma_c$  have been derived within  $0.1a_e$ . These velocity dispersion values are also listed in Table 4. The central dispersions derived here can be compared with those derived by other authors, for those five galaxies for which such a measure has been made (see Table 1). The agreement is excellent for NGC 3258 and NGC 3923, and good within the errors for NGC 2563 and NGC 3078: the values of  $\sigma_c$  in Table 1 for these two galaxies have been derived from those of Davies et al. 1987, who find respectively  $\sigma_c = 261 \pm 26$  and  $\sigma_c = 238 \pm 24$ . The lower  $\sigma_c$  we

**Table 4.** Rotational velocities and velocity dispersions

Galaxy	$\sigma_c$	$\langle\sigma\rangle$	$\Delta R$	$v_{rot}$	R	$v_{fit}$
(1)	km s <sup>-1</sup>	km s <sup>-1</sup>	''	km s <sup>-1</sup>	''	km s <sup>-1</sup>
N2563	278.9±9.4	263.5±6.7	9–28	109±21	25	119
N2563 <sup>a</sup>	260.5±16.6	236.2±10.7	-11–7	0±8		
N3078	263.5±8.4	253.8±5.8	15–34	76±18	30	93
N3258	274.5±7.2	242.2±5.9	3–20	40±6	20	41
N3923	248.8±6.0	244.4±4.6	-24–23	1±4		
N4526	209.8±2.7	190.2±2.3	50–135	246±6		
N4753	166.9±3.1	149.8±2.9	20–70	127±8	60	153
N4756	203.9±12.0	203.8±8.3	4–11	34±13	11	31

Notes – Col. (2) gives the central (i.e., averaged within  $0.1a_e$ ) velocity dispersion; col. (3) gives the mean velocity dispersion along the major axis (also the minor axis for NGC 2563), calculated as average within  $0.5a_e$ . All the data points have been given equal weight. Col. (4) gives the radial interval over which the radial velocities have been averaged; the error weighted mean rotational velocities over that interval are given in col. (5). The radial velocity at the outermost point of the model fit – in col. (6) – is given in col. (7), when this fit is acceptable. <sup>a</sup> minor axis.

**Figure 2.** Panel a shows  $L_X/L_B$  versus  $v_{rot}/\sigma_c$ , with  $L_X$  in erg s<sup>-1</sup> from Fabbiano et al. (1992);  $L_B$  is in  $L_\odot$ , and the values have been derived using  $B_T^0$  from RC3, and the distances given in Fabbiano et al. (1992). In panel b the ratio  $L_X/L_B$  is plotted against the apparent ellipticity  $\epsilon = 1 - b/a$ ;  $b/a$  values are from RC3. Open circles are Es, and full circles are S0s.

find for NGC 4526 is due to the larger region used by us to estimate it.

Only one galaxy (NGC 3923) does not show significant rotation along the major axis; for this object we calculate  $v_{rot}$  as the weighted average of all values within a radius of  $20''$ .

## 6 DISCUSSION

### 6.1 X-ray emission, galaxy shape and internal kinematics

#### 6.1.1 X-ray emission, rotation and flattening

We collect in Table 5 the kinematic properties of the Fabbiano et al. (1992) sample of early-type galaxies with X-ray detection and measured rotational velocity along the major axis. Including the objects studied in the present work, 52 galaxies have both  $\sigma_c$  and  $v_{rot}$  measured. This is the first large sample of early-type galaxies with detected X-ray emission and known kinematics, and it is used here to investigate from an observational point of view the effect of rotation and flattening on  $L_X$ .

In Fig. 2 we plot  $L_X/L_B$ , a measure of the hot gas content of the galaxies, versus  $v_{rot}/\sigma_c$ , an indicator of the

**Figure 3.** The relation between  $L_X/L_B$  and  $L_B$ .  $L_X$  and  $L_B$  are estimated as in Fig. 2; also the symbols are the same.

importance of rotation, and  $L_X/L_B$  versus the ellipticity  $\epsilon = 1 - b/a$ , for Es and S0s separately. We note the following:

1) Both morphological types populate the whole range of  $L_X/L_B$ , i.e., no morphological segregation in  $L_X/L_B$  is present. S0s, though, are preferentially found at low or intermediate  $L_X/L_B$ , while Es are more homogeneously distributed (in agreement with the findings of EFKa<sup>†</sup>).

2) The trend between  $L_X/L_B$  and  $v_{\text{rot}}/\sigma_c$  (Fig. 2a) is L-shaped, with the X-ray brightest objects confined at  $v_{\text{rot}}/\sigma_c \lesssim 0.4$ , both for Es and S0s. As expected, Es are found at lower rotations with respect to S0s.<sup>‡</sup> Neither for low or intermediate X-ray to optical ratio, say  $\log(L_X/L_B) \lesssim 30.2$ , nor for high  $L_X/L_B$ , there is any clear correlation between X-ray emission and rotational properties.

3) In our sample of X-ray emitting galaxies the trend discovered by EFKb is still present as an L-shape in Fig. 2b, (reminiscent of that in Fig. 2a): there are no high  $L_X/L_B$  objects with high  $\epsilon$ . Again, no clear correlations with  $\epsilon$  are present, just a confinement of Es at lower flattenings with respect to S0s.

Are the trends of  $L_X/L_B$  with  $v_{\text{rot}}/\sigma_c$  and  $\epsilon$  produced by the underlying correlation  $L_X \propto L_B^2$  (even though this has a very large scatter)? It could be that fast rotators and flat galaxies are found at low  $L_X/L_B$  because they are also preferentially at low  $L_B$ . Fig. 3 shows that this is not the case: in our sample there is no relationship between  $L_X/L_B$  and  $L_B$ , neither for Es nor for S0s (as already found by EFKa); moreover, S0s and Es span the same range in  $L_B$ .

Fig. 2 displays projected quantities, not corrected for the inclination of the galaxies along the line of sight. To test the effect of inclination, we correct  $v_{\text{rot}}/\sigma_c$  of the S0 subsample using an inclination angle estimated on the hypothesis of an intrinsic  $b/a = 0.25$  (Dressler & Sandage 1983), and that S0s are isotropic rotators, which gives the maximum correction on the projected  $v_{\text{rot}}/\sigma_c$  (see Binney & Tremaine 1987). After this correction the L-shape in Fig. 2a is preserved, with small shifts towards higher  $v_{\text{rot}}/\sigma_c$  for most of the S0s. The analogous correction for the ellipticals cannot be made, because there are no obvious ways to derive even approximate inclination angles.

<sup>†</sup> The analysis conducted by EFKa,b is based on 146 objects, including detections and upper limits on X-ray fluxes.

<sup>‡</sup> 4 S0s and 6 Es with X-ray detection still lack any measure of rotation along the major axis (in addition to 5 face-on S0s). These Es missing in Fig. 2 have  $\log(L_X/L_B) > 30.2$ , and  $L_B \gtrsim 9 \times 10^{10} L_\odot$ , except one at  $L_B = 6 \times 10^{10} L_\odot$ . So, they would probably turn out to be slowly rotating objects, in the upper left portion of Fig. 2a.

**Figure 4.** The relation between  $L_X/L_B$  and the anisotropy parameter  $(v/\sigma)^*$  (see Section 6.1.2). Es are open circles and S0s full circles.  $\langle \sigma \rangle$  has been published for 46 galaxies only; the plot with  $\sigma_c$  replacing  $\langle \sigma \rangle$ , and so containing all the 52 galaxies in our sample, is basically the same.

**Figure 5.** The relation between  $v_{\text{rot}}/\sigma_c$  and ellipticity for the Es (open circles) and S0s (full circles) in our sample.

### 6.1.2 X-ray emission, orbital anisotropy and inner isophotal shape

Another useful investigation is the analysis of the relationship between X-ray emission, orbital anisotropy, and the presence of inner stellar disks, that is evidenced by deviations from pure elliptical isophotes (the  $a_4/a$  parameter introduced by Bender et al. 1989). Anisotropy and presence of disks are believed to give information on the internal structure of a galaxy and its formation history, and so they might have a relationship with the X-ray emission. Bender (1990) has discussed the relevance of isophote shape studies for the understanding of the structure of early-type galaxies. When making a statistical analysis of a large sample of objects with  $\log L_B > 10.2$ , no relation between  $L_B$  and  $\epsilon$ , or  $L_B$  and anisotropy is observed, and only a weak correlation between  $a_4/a$  and  $L_B$  or  $\epsilon$  is present, but a clear dependence of anisotropy and of  $L_X$  on  $a_4/a$  is found: disky objects are low X-ray emitters, and in general flattened by rotation; boxy and irregular objects (likely merger remnants, or objects that have suffered accretion and interaction events, Nieto 1989) show a large range of  $L_X$ , and various degrees of velocity anisotropy. The relationship between X-ray emission and  $a_4/a$  has been reanalyzed by EFKb using their larger sample: the bivariate correlation analysis of  $L_B$ ,  $L_X$ ,  $L_X/L_B$  with  $a_4/a$  confirms the finding that X-ray luminous galaxies tend to be boxier than X-ray faint ones; the trend with  $L_X/L_B$ , in the sense that there is less hot gas in disky objects, is the weakest of the three.

Following Davies et al. (1983), we estimate the amount of anisotropy by calculating the quantity  $(v/\sigma)^*$ , that is the ratio between the observed  $v_{\text{rot}}/\langle \sigma \rangle$  and  $(v_{\text{rot}}/\langle \sigma \rangle)_{\text{OI}}$ , which is the value for an oblate isotropic rotator with the same ellipticity ( $\langle \sigma \rangle$  is the average within  $0.5R_e$ ). Although radial changes of  $\epsilon$  may produce some inaccuracies in the estimate of  $(v/\sigma)^*$ , in objects with  $(v/\sigma)^* \lesssim 0.7$  velocity dispersion

**Table 5.**  $v_{\text{rot}}$  and  $\sigma_c$  for the X-ray sample

Galaxy	$\sigma_c$	$v_{\text{rot}}$	Galaxy	$\sigma_c$	$v_{\text{rot}}$
(1)	km s <sup>-1</sup>	km s <sup>-1</sup>	(4)	km s <sup>-1</sup>	km s <sup>-1</sup>
(1)	(2)	(3)	(4)	(5)	(6)
NGC 315	300	15	NGC 4374	296	10
NGC 533	301	20	NGC 4382	192	60
NGC 720	243	27	NGC 4406	250	8
NGC 1052	222	92	NGC 4458	106	20
NGC 1316	243	135	NGC 4472	303	73
NGC 1332	332	225	NGC 4473	193	54
NGC 1395	245	100	NGC 4526	267	246
NGC 1399	308	27	NGC 4552	269	1.3
NGC 1404	250	90	NGC 4636	207	1.7
NGC 1407	272	47	NGC 4638	132	130
NGC 1553	200	150	NGC 4649	339	87
NGC 1600	342	7.1	NGC 4697	181	101
NGC 2300	254	5	NGC 4753	167	127
NGC 2563	260	109	NGC 4756	204	34
NGC 2832	310	8	NGC 4762	147	165
NGC 2974	201	191	NGC 5077	273	15
NGC 3078	237	76	NGC 5084	211	200
NGC 3258	271	40	NGC 5363	198	140
NGC 3585	218	45	NGC 5838	290	225
NGC 3607	241	108	NGC 5846	252	2
NGC 3608	203	43	NGC 5866	174	132
NGC 3923	241	1.0	NGC 5982	256	60
NGC 4168	186	20	NGC 7619	312	65
NGC 4261	326	3	NGC 7626	273	10
NGC 4291	278	68	IC 4296	316	36
NGC 4365	261	5	IC 1459	316	28

Notes – Cols. (2) and (5) give the central velocity dispersion from McElroy (1995), cols. (3) and (6) give the rotational velocities. References for cols. (3) and (6) are Bender et al. (1992), Bertola & Capaccioli (1978), Bender et al. (1994), Bertola et al. (1991), Carter (1987), Davies et al. (1983), Davies & Birkinshaw (1988), D’Onofrio et al. (1995), Dressler & Sandage (1983), Fried & Illingworth (1994), Fisher et al. (1995), Franx et al. (1989), Oosterloo et al. (1994), Prugniel & Simien (1994), Scorza & Bender (1995), Seifert & Scorza (1996).

anisotropies are likely to be present (Bender 1988). In Fig. 4 we show the relationship between  $L_X/L_B$  and  $(v/\sigma)^*$  for our sample: there is no clear trend, in particular the L-shape present in Fig. 2a has disappeared. This is not completely surprising: the effect of using  $(v/\sigma)^*$  instead of  $v_{\text{rot}}/\sigma_c$  is that of populating the upper right region of the diagram, because some round, slowly rotating objects can have the anisotropy parameter close to unity. On the other hand, flat objects with high rotation (i.e., lying in the lower right region of Fig. 2a) might require some anisotropy to maintain their flattening, and so they are moved towards the lower left region in Fig. 4. So, the observations suggest that the major effect on  $L_X/L_B$  is not given by anisotropy, but it is given by the relative importance of rotation and random motions.

For what is concerning a possible role of the isophotal shape,  $a_4/a$  has been measured for only 28 galaxies of our sample, and for all of them  $a_4/a \cdot 100 \lesssim 1.4$ . This subsample shows only a marginal trend of  $L_X/L_B$  with  $a_4/a$ , in the same sense as that found by EFKb, which is in fact mainly produced by those few galaxies with  $1.2 < a_4/a \cdot 100 < 2.8$ . Since the subsample with measured  $a_4/a$  is limited to  $v_{\text{rot}}/\sigma_c \lesssim 0.5$ , we cannot discuss whether the dynamical and/or structural reason of boxiness and diskiness has some

relationship with the origin of the threshold effects produced by rotation and ellipticity in Fig. 2. We can only recall that EFKb do not find a threshold effect as that present in Fig. 2, when considering the role of  $a_4/a$  for their sample. Only when a considerably larger sample of galaxies with observed  $L_X$  and  $v_{\text{rot}}$  will be available, and a robust multivariate analysis will be possible, some stronger conclusions can be obtained.

## 6.2 Comparison with theoretical predictions

Recently three different theoretical works have studied the problem of the effect of rotation, and of the shape of the mass distribution, on X-ray gas flows. The results of these investigations (CP; BM; D’Ercole & Ciotti 1996) are summarized below.

1) Within the WOI scenario that explains the scatter in the  $L_X - L_B$  diagram in terms of different flow phases for the hot gas, CP relate the gas flow phase (and so  $L_X$ ) to the rotational and gravitational properties of the host galaxies. They compare the energy budget of the gas in spherical and in flattened/rotating galaxies of the same  $L_B$  (and so of the same SNIa heating). They find that the flattening can

**Figure 6.** The trend with  $v_{\text{rot}}/\sigma_c$  of the residuals from the best fit of the  $L_X - L_B$  correlation determined by EFKa, for our sample (Es are open circles, S0s are full circles).

be effective in unbounding the hot gas; on the contrary, for a given galaxy structure, rotation cannot change a bound gaseous halo into an unbound one. So, CP conclude that S0s and non-spherical Es are less able to retain hot gaseous haloes than are rounder systems of the same  $L_B$ ; i.e., more likely they are in the outflow or wind phase. This result looks quite attractive because it can explain the X-ray underluminosity of flatter systems within the class of *both* S0s and Es (the findings of EFKa,b), while ellipticals are slower rotators than S0s. An important consequence of the CP explanation is to predict *not correlation* but *segregation* of  $L_X/L_B$  with respect to the flattening, a feature visible in Fig. 2b, at least for S0s. This segregation is produced by the fact that at each  $L_B$  there is a critical  $\epsilon$  such that all the flatter objects are in outflow/wind, rounder ones are in inflow.

2) Two-dimensional numerical simulations of gas flows in non spherical early-type galaxies have been carried out by BM. They consider oblate galaxies of different axial ratios, sustained by different amounts of ordered and disordered kinetic energies, and a present SNIa rate of one tenth of the value given by Tammann (1982). The resulting flows are always in the inflow phase, and form a massive, cold disk.  $L_X$  is reduced in rotating models, because the angular momentum prevents the cooling gas from falling directly to the bottom of the potential well, and the gas cools before entering the galactic core region. In this scenario  $L_X$  marginally depends on the flatness of the galaxy (in agreement with the CP calculations applied to the inflow case), while models with the same  $L_B$  have a range in  $L_X/L_B$  of over an order of magnitude, going from non rotating objects to E2 galaxies with  $v_{\text{rot}}/\sigma_c = 0.66$ , or to E4 galaxies with  $v_{\text{rot}}/\sigma_c = 0.78$ . BM so suggest that most of the spread observed in the  $L_X - L_B$  plane could be due to rotation, and that rotation is the underlying cause of the X-ray underluminosity of flat objects found by EFKb, because it increases on average with  $\epsilon$ , as shown in Fig. 5 for our sample. They predict that  $v_{\text{rot}}/\sigma_c$  should correlate with the residuals in the  $L_X - L_B$  plot. We show in Fig. 6 the trend of these residuals with  $v_{\text{rot}}/\sigma_c$ : a very weak trend with a large spread is perhaps present for S0s.

3) D’Ercole & Ciotti (1996) perform two-dimensional numerical simulations of gas flows for S0s, in the WOI scenario. Luminous and dark matter densities, and their internal dynamics are the same as in CP. Models without SNIa heating give qualitatively the BM’s results. Models with SNIa at 0.3 the Tammann’s rate, both with and without rotation, accumulate negligible amounts of cold gas on a central disk, and very soon develop a partial wind that lasts tens of Gyrs; if spherical, these models would be in inflow. Rotation decreases the X-ray emission slightly (of a factor

of two or so), because it just favours the wind, as predicted by CP. The conclusion is that flat models, rotating or not, can be significantly less X-ray luminous than spherical ones of the same  $L_B$ , because they are in partial wind when the spherical ones are in inflow; rotation has a minor effect.

## 7 CONCLUSIONS

Which predictions of the previous scenarios find support in our observational findings? The existence of a relation between  $v_{\text{rot}}/\sigma_c$  and  $\epsilon$  (Fig. 5) makes it difficult to determine whether rotation or flattening produces the trends in Fig. 2. We can at least consider whether in the data there is some trace of the effect that rotation and flattening are predicted to have in the pure inflow and in the WOI scenarios: flattening has no importance in the first (BM), while it is determinant in the second (CP; D’Ercole & Ciotti 1996).

In the assumption that all galaxies host an inflow, rotation alone cannot explain the whole observed spread of more than two orders of magnitude in  $L_X$ : BM predict a spread of roughly one order of magnitude by requiring  $v_{\text{rot}}/\sigma_c$  up to 0.78, a value quite larger than that shown by the ellipticals in the X-ray sample (Fig. 2a). Moreover, as discussed in Section 6.2, the expected correlation of  $L_X/L_B$ , or of the residuals of the  $L_X - L_B$  correlation, with  $v_{\text{rot}}/\sigma_c$  is not present (Fig. 2a and 6).

On the other hand, the trend between  $L_X/L_B$  and  $\epsilon$  could be in agreement with the predictions of CP and D’Ercole & Ciotti (1996), because of the threshold effect present in Fig. 2b. The trend of  $L_X/L_B$  and  $v_{\text{rot}}/\sigma_c$  could be produced by the correlation between  $v_{\text{rot}}/\sigma_c$  and  $\epsilon$ . It remains unexplained why the L-shape is more pronounced with respect to  $v_{\text{rot}}/\sigma_c$  rather than to  $\epsilon$ : below  $\log(L_X/L_B) \approx 30.2$  there are more objects with  $v_{\text{rot}}/\sigma_c > 0.4$  rather than with  $\epsilon > 0.5$ .

We have also checked whether there is any relationship in our sample between X-ray emission, orbital anisotropy, and the presence of inner stellar disks. We have not found any threshold effect, or significant correlations, between  $L_X/L_B$  and anisotropy or isophotal shape.

So, we conclude that a satisfactory explanation of all the features in Fig. 2 is not given by any of the two scenarios above. A partial interpretation could be as follows:

- at low  $L_X/L_B$ , flat galaxies contribute substantially to the total number of objects, because of the importance of flattening, that makes the partial wind phase favoured.
- at high  $L_X/L_B$ , where galaxies are in inflow, the scatter in  $L_X$  could be due, at least partially, to rotation, as suggested by BM.

Finally, we note that Fig. 2 argues against the hypothesis that some peculiar properties of the stellar population of S0s with respect to that of Es (e.g., a higher SNIa rate, or a younger/bluer stellar population) could be responsible for lowering the  $L_X/L_B$  ratio: at low rotations and at low flattenings, where the two morphological types overlap, S0s span the same range of  $L_X/L_B$  as Es.

## ACKNOWLEDGMENTS

We thank J. Binney, F. Brighenti, A. D’Ercole and G. Galletta for useful discussions, and the referee for suggestions that helped improve the paper.

**REFERENCES**

- Bender R., 1988, *A&A*, 193, L7
- Bender R., Surma P., Döbereiner S., Möllenhoff C., Madejsky R., 1989, *A&A*, 217, 35
- Bender R., 1990, *Dynamics and Interactions of Galaxies*, ed. R. Wielen (Berlin: Springer Verlag), p. 232
- Bender R., Burstein D., Faber S.M., 1992, *ApJ*, 399, 462
- Bender R., Saglia R.P., Gerhard O.E., 1994, *MNRAS*, 269, 785
- Bertola F., Bettoni D., Danziger J., Sadler E., Sparke L., de Zeeuw T., 1991, *ApJ*, 373, 369
- Bertola F., Capaccioli M., 1978, *ApJ*, 219, 404
- Binney J., Tremaine S., 1987, *Galactic Dynamics*, Princeton Univ. Press, Princeton, p. 216
- Brighenti F., Mathews W.G., 1996, *ApJ*, in press (BM)
- Carter D., 1987, *ApJ*, 312, 514
- Ciotti L., Pellegrini S., 1996, *MNRAS*, 279, 240 (CP)
- Ciotti L., D'Ercole A., Pellegrini S., Renzini A., 1991, *ApJ*, 376, 380
- Davies R.L., Efstathiou G., Fall M., Illingworth G., Schechter P., 1983, *ApJ*, 266, 41
- Davies R. L., Burstein D., Dressler A., Faber S.M., Lynden-Bell D., Terlevich R.J., Wegner G., 1987, *ApJS*, 64, 581
- Davies R.L., Birkinshaw M., 1988, *ApJS*, 68, 409
- D'Ercole A., Ciotti L., 1996, *ApJ*, submitted
- de Vaucouleurs G., de Vaucouleurs A., Corwin Jr. H.G., Buta R.J., Paturel G., Fouque P., 1991, *Third Reference Catalogue of Bright Galaxies*, (New York: Springer Verlag) (RC3)
- D'Onofrio, M., Zaggia, S., Longo, G., Caon, N., Capaccioli, M., 1995, *A&A*, 296, 319
- Dressler A., Sandage A., 1983, *ApJ*, 265, 664
- Eskridge P., Fabbiano G., Kim D.W., 1995a, *ApJS*, 97, 141 (EFKa)
- Eskridge P., Fabbiano G., Kim D.W., 1995b, *ApJ*, 442, 523 (EFKb)
- Fabbiano G., 1989, *ARA&A*, 27, 87
- Fabbiano G., Kim D.W., Trinchieri G., 1992, *ApJS*, 80, 531
- Fisher D., Illingworth G., Franx M., 1995, *ApJ*, 438, 539
- Franx M., Illingworth G., Heckman T., 1989, *ApJ*, 344, 613
- Fried J.W., Illingworth G., 1994, *AJ*, 107, 992
- Kim D.W., Fabbiano G., Trinchieri G., 1992, *ApJ*, 393, 134
- Kley W., Mathews W.G., 1995, *ApJ*, 438, 100
- McElroy D.B., 1995, *ApJS*, 100, 105
- Nieto J.L., 1989, 2<sup>da</sup> Reunion de Astronomia Extragalactica, *Bul. Academia Nacional de Ciencias de Cordoba*, 58, 239
- Oosterloo T., Balcells M., Carter D., 1994, *MNRAS*, 266, L10
- Prugniel P., Simien F., 1994, *A&A*, 282, L1
- Sandage A., Tammann G.A., 1987, *A Revised Shapley-Ames Catalogue of Bright Galaxies*, Washington, Carnegie Institute
- Scorza C., Bender R., 1995, *A&A*, 293, 20
- Seifert W., Scorza C., 1996, *A&A*, 310, 75
- Tammann G.A., 1982, *Supernovae: A Survey of Current Research*, eds. M. Rees and R. Stoneham (Dordrecht: Reidel), p. 371
- Tully B., 1988, *Nearby Galaxies Catalog*, (New York: Cambridge Univ. Press)
- White R.E., III, Sarazin C.L., 1991, *ApJ*, 367, 476

**APPENDIX A: KINEMATIC DATA**

The kinematic results for our program galaxies are tabulated here. The derived radial velocities  $v$  and velocity dispersions  $\sigma_c$  along with their formal errors ( $\pm 1\sigma$ ) are given, in  $\text{km s}^{-1}$ . Radii are in arcseconds. The position angles in degrees, PA, are consistent with the normal convention, increasing from north to east.

## NGC 2563 PA 80 major axis

R(")	$v$	$\Delta v$	$\sigma$	$\Delta\sigma$
-14.3	119.6	65.9	200.0	57.7
-8.1	54.5	33.9	200.0	29.7
-5.1	98.3	39.5	248.0	50.5
-3.0	104.1	19.7	278.4	25.2
-1.5	23.0	22.4	248.0	28.7
-0.7	-5.3	19.1	301.7	24.6
0.1	-17.5	17.2	262.6	22.0
0.9	-12.1	14.8	300.3	19.0
1.7	-34.2	12.8	282.0	16.4
2.9	-46.7	11.9	269.9	15.2
4.5	-62.5	17.2	229.2	22.0
6.1	-84.1	25.3	233.2	32.3
8.1	-67.6	38.7	308.4	49.8
11.5	-94.8	40.5	225.5	51.8
17.1	-124.6	43.7	204.3	56.0
27.4	-99.3	75.0	200.0	65.6

## NGC 2563 PA 90 minor axis

R(")	$v$	$\Delta v$	$\sigma$	$\Delta\sigma$
-11.2	-45.2	60.4	173.2	77.8
-6.1	-8.6	33.9	153.5	43.9
-3.0	-44.5	26.3	251.0	33.8
-1.2	-28.9	18.4	248.0	23.6
0.4	-17.4	18.1	273.0	23.3
2.0	-67.0	16.1	272.3	20.7
3.9	-40.8	24.0	233.6	30.8
6.9	-42.2	48.9	222.1	62.8

## NGC 3078 PA 177 major axis

R(")	$v$	$\Delta v$	$\sigma$	$\Delta\sigma$
-34.4	55.9	46.5	172.86	77.37
-27.1	35.9	62.9	174.09	87.04
-21.4	26.3	62.4	281.2	81.2
-15.6	72.2	45.4	266.5	59.0
-10.8	64.9	25.8	274.1	33.6
-7.2	101.9	21.1	254.6	27.5
-4.9	78.9	15.3	244.9	19.8
-3.3	71.4	11.3	252.9	14.7
-1.7	40.4	11.1	271.6	14.4
-0.1	5.0	10.8	272.1	14.0
1.5	-38.2	11.7	246.7	15.2
3.1	-57.6	15.7	291.8	20.5
4.7	-76.1	18.9	225.1	24.5
6.7	-91.1	20.0	231.1	26.0
9.8	-70.1	24.2	226.38	42.65
14.9	-82.4	45.8	269.43	85.34
23.1	-92.2	56.5	257.9	129.0
34.4	-111.5	36.9	105.2	47.7

This paper has been produced using the Royal Astronomical Society/Blackwell Science  $\text{\TeX}$  macros.



NGC 3258 PA 75 major axis

R(")	$v$	$\Delta v$	$\sigma$	$\Delta\sigma$
-20.4	24.1	33.0	154.6	44.7
-13.4	42.6	25.1	172.9	34.2
-8.6	66.2	20.0	210.6	27.5
-6.0	25.8	24.0	256.0	32.6
-4.4	46.4	18.5	302.5	24.6
-2.8	32.9	12.1	282.7	16.3
-1.2	54.4	12.0	316.5	15.9
0.0	-0.9	13.4	281.2	18.0
1.2	-27.9	10.5	250.4	14.2
2.8	-41.5	12.9	241.4	17.6
4.7	-37.0	13.8	199.9	19.0
7.2	-45.6	20.3	230.6	27.8
11.0	-36.1	22.0	161.4	29.8
16.8	-48.5	50.6	140.0	49.7

NGC 3923 PA 50 major axis

R(")	$v$	$\Delta v$	$\sigma$	$\Delta\sigma$
-30.1	-44.2	43.5	262.6	96.7
-24.1	9.8	26.4	246.5	34.1
-17.9	20.9	20.5	258.7	30.8
-12.8	8.7	17.4	248.9	21.5
-9.7	24.1	19.8	247.6	25.7
-6.3	4.5	13.2	252.4	13.3
-3.6	5.4	10.0	245.6	14.7
-2.0	-9.7	11.0	261.9	14.1
-0.4	-13.8	9.7	252.6	12.4
1.2	-8.5	10.8	243.4	13.9
3.2	-8.1	10.8	245.1	13.8
6.3	6.9	12.2	233.9	15.7
11.1	25.7	15.0	237.5	19.2
16.8	-4.5	25.3	282.4	32.4
22.5	28.9	30.4	224.1	38.9
28.2	53.8	38.1	166.7	49.2

NGC 4526 PA 113 major axis

R(")	$v$	$\Delta v$	$\sigma$	$\Delta\sigma$
-135.4	216.0	50.8	124.8	81.0
-116.7	183.1	47.0	28.1	56.8
-101.7	251.6	58.3	0.9	116.9
-88.7	266.4	34.5	32.8	47.6
-76.5	256.2	25.3	89.2	32.1
-64.3	202.9	19.2	71.3	24.4
-53.5	245.3	14.4	72.0	18.4
-45.5	200.6	26.4	163.5	36.0
-39.4	155.4	33.1	198.8	45.6
-33.7	132.4	22.8	162.2	31.1
-28.5	153.0	30.2	193.9	41.6
-23.4	132.2	17.2	179.7	23.6
-15.6	144.5	11.6	167.6	15.8
-11.9	175.1	8.9	156.7	12.0
-7.9	170.2	13.7	186.0	18.9
-7.1	175.0	11.1	178.9	15.3
-6.3	179.4	9.9	173.5	13.5
-5.5	165.2	9.3	182.1	12.7
-4.7	154.9	8.9	199.6	12.2
-3.9	127.3	8.2	192.0	11.3
-3.1	112.8	7.8	205.1	10.7
-2.3	86.1	7.2	216.2	10.0
-1.4	51.4	7.8	253.6	10.7
-0.6	28.5	7.8	245.8	10.8
0.2	0.0	7.5	222.0	10.4
1.0	-23.6	7.4	243.8	10.2
1.8	-47.1	8.8	219.9	12.1
2.6	-70.9	8.4	231.2	11.6
3.4	-69.8	9.1	219.0	12.5
4.2	-118.7	7.8	186.6	10.8
5.0	-136.1	9.4	216.3	13.0

NGC 4526 PA 113 major axis – *continued*

R(")	$v$	$\Delta v$	$\sigma$	$\Delta\sigma$
5.8	-143.4	9.3	188.8	12.8
6.7	-168.2	10.7	220.9	14.7
7.5	-147.6	11.4	190.4	15.7
8.3	-155.1	12.0	207.7	16.5
9.1	-186.2	10.5	142.5	14.2
9.9	-147.8	16.3	197.3	22.4
10.7	-144.4	16.6	189.1	22.9
12.3	-114.4	17.6	192.6	24.3
13.1	-141.6	20.4	168.0	27.9
16.8	-140.1	16.5	174.8	22.6
18.4	-161.8	18.0	180.4	24.8
20.4	-106.8	15.9	155.0	21.7
22.8	-83.8	18.3	163.0	25.0
26.0	-101.4	16.5	183.3	22.6
30.1	-158.2	21.7	192.8	29.9
34.1	-170.5	16.3	123.6	21.9
38.2	-195.7	23.3	115.2	30.8
42.2	-189.6	22.5	138.6	30.2
46.3	-230.0	29.5	135.1	39.8
51.5	-250.4	21.1	120.8	28.0
57.6	-192.8	23.3	125.9	31.1
62.9	-292.2	42.3	122.9	56.2
68.5	-238.9	22.5	74.8	28.7
75.1	-280.4	27.4	0.4	36.9
81.1	-270.1	27.8	187.0	54.8
87.2	-273.3	21.4	53.0	29.4
94.0	-247.2	27.2	13.1	83.2
101.3	-251.5	30.2	60.0	27.6
109.0	-303.7	34.4	60.8	20.6
118.9	-252.1	29.6	60.8	39.1
131.1	-288.5	57.2	60.0	62.7

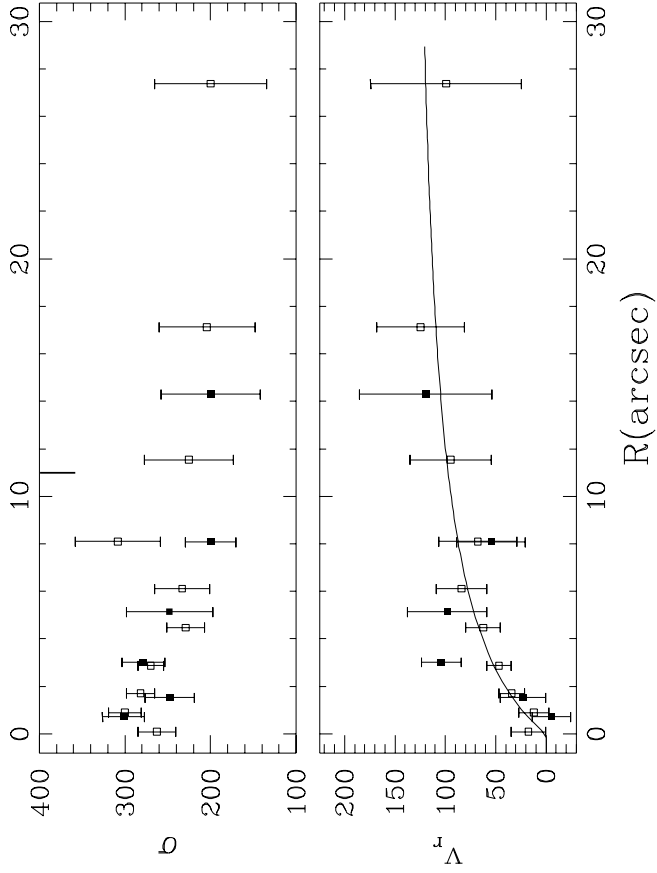
## NGC 4753 PA 80 major axis

R(")	$v$	$\Delta v$	$\sigma$	$\Delta\sigma$
-70.0	-186.6	95.8	80.1	99.2
-58.4	-163.9	58.0	99.1	74.8
-48.7	-129.9	33.9	100.1	34.6
-41.0	-129.0	23.0	93.7	29.9
-32.9	-152.7	26.5	124.0	35.4
-26.1	-144.6	20.1	100.0	20.6
-21.3	-134.1	26.5	142.3	35.7
-16.8	-131.3	19.6	154.2	26.6
-11.9	-118.7	21.4	171.1	29.3
-7.3	-98.4	13.5	169.3	18.4
-5.8	-104.3	12.0	154.8	16.4
-3.9	-101.9	9.3	160.6	12.6
-2.7	-54.3	10.6	163.0	12.1
-1.9	-31.8	7.1	169.6	10.9
-1.1	-37.7	7.5	171.0	10.2
-0.3	-17.0	6.6	163.8	10.5
0.5	2.6	6.2	165.3	8.4
1.3	21.6	6.7	172.6	10.3
2.1	60.0	7.2	172.4	9.8
3.0	75.5	9.4	168.4	12.9
3.8	92.2	12.4	176.0	13.2
5.0	105.9	8.6	173.0	11.0
6.6	125.9	12.8	159.6	17.4
9.4	128.0	14.2	159.4	19.4
11.8	147.2	21.5	160.1	29.2
14.2	155.8	20.4	131.7	27.4
17.1	122.7	18.6	104.9	24.4
21.1	123.8	17.3	117.8	23.0
26.0	111.7	18.9	95.4	24.6
30.8	125.1	22.8	93.3	24.4
35.6	117.8	17.2	82.9	21.6
41.8	134.6	34.6	118.9	33.1
49.7	115.5	44.6	70.7	35.4
60.5	90.6	48.7	119.1	65.8
74.1	112.2	41.3	99.0	49.5

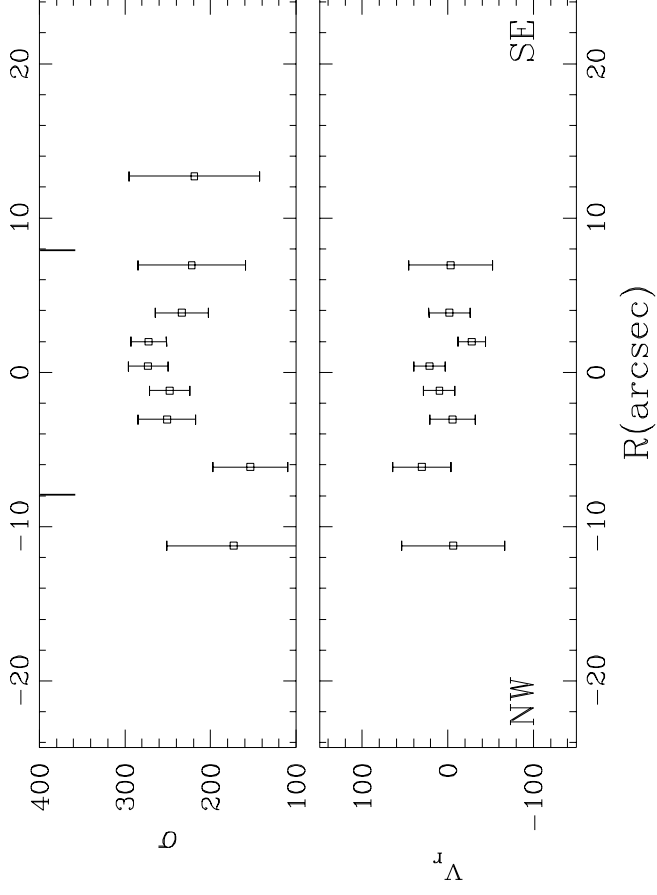
## NGC 4756 PA 50 major axis

R(")	$v$	$\Delta v$	$\sigma$	$\Delta\sigma$
-10.5	47.9	32.3	210.8	45.3
-4.6	45.2	22.9	193.3	32.0
-2.4	11.4	15.3	207.8	21.4
-0.8	20.1	12.9	206.6	18.1
0.8	-18.2	11.4	201.3	15.9
2.4	-29.3	14.8	194.2	20.6
7.4	-22.9	17.5	212.5	24.9

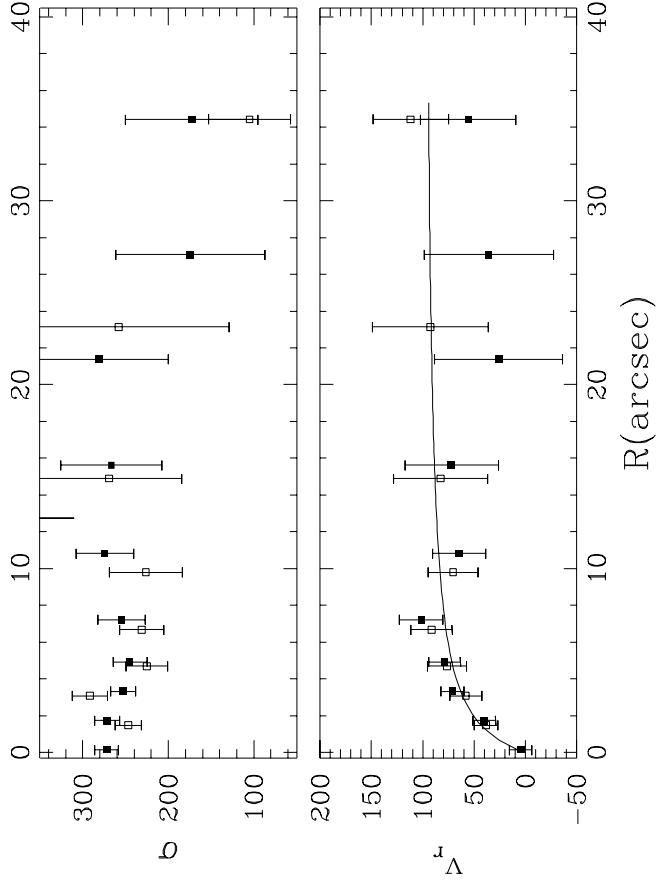
NGC2563 major axis



NGC2563 minor axis



NGC3078



NGC3258

